Journal of Materials Chemistry B

ROYAL SOCIETY OF CHEMISTRY

PAPER

View Article Online
View Journal



Cite this: DOI: 10.1039/d6tb00302h

# Low-molecular weight organogel matrices as crystallisation media for active pharmaceutical ingredients

Alarqam Zyaad Tareq,[ab] Matthew Hyder,[a] Ann M. Chippindale,[a] Nicholas J. Spencer,[a] Saeed D. Mohan,[c] Amanpreet Kaur,[c] James E. Hallett,[a] Thomas Zinn,[d] Kenneth Shankland[e] and Wayne Hayes *[a]

Received 5th February 2026,
Accepted 16th March 2026

DOI: 10.1039/d6tb00302h

rsc.li/materials-b

The vast majority of small-molecule active pharmaceutical ingredients (APIs) are formulated in the crystalline state, for reasons including thermodynamic stability, ease of purification and characterisation, and better control over polymorphism. However, the selective crystallisation of polymorphic APIs provides a significant hurdle to overcome, especially in the case of API co-crystals. Herein we report a series of low-molecular-weight organogels (LMWGs) which can be used to selectively crystallise APIs. In solution, these LMWGs (2–10 mg mL$^{-1}$) self-assemble through hydrogen bonding to form stable gels which feature nano-structured morphologies. When utilised as crystallisation media, these LMWGs can influence crystal growth, as evidenced by the discovery of two novel 1 : 1 co-crystals of chlorzoxazone with nicotinamide and chlorzoxazone with isonicotinamide. This work highlights the potential of LMWGs as another means of controlling API crystallisation.



## Introduction

The self-assembly of low-molecular-weight supramolecular materials *via* non-covalent interactions generates dynamic systems[1,2] capable of stimulus-response behaviour[3] triggerable upon exposure to light,[4] temperature,[5] pH,[6] or chemical redox processes.[7] Low-molecular-weight gelators (LMWGs) are formed though hierarchical self-assembly of small molecules into one-dimensional structures in both organic and aqueous media.[8,9] These assemblies can then cross-link to generate various structural architectures, including three-dimensional (3D) networks that extend into fibrils at the nano- or microscale yielding fibrous, tubular, or helical aggregates.[9–11]

In 1997, Terech and Weiss described the generation of supramolecular gels,[9] and reported a series of thermally reversible low-molecular-weight organogelators that feature urea or thiourea functional groups at chain ends or within the chains of *n*-alkanes. Hydrogen bonds have been found to play a vital role in the development and assembly of numerous organogelators; a variety of functional groups such as alcohols,[12] ureas[13] and amides[14–16] have been utilised successfully to afford low-molecular-weight organogels.[17] Urea and amide groups are effective at forming hydrogen-bonding motifs owing to the N–H donor and carbonyl acceptor groups.[18–20] The ability of these functional groups to form strongly-associating, self-complementary, and directional hydrogen bonds in tandem with other intermolecular interactions, such as van der Waals' forces, affords stability to the LMWGs nanostructures in different bulk media.[14,21,22] Notably, novel low-molecular-weight gelators have been reported by Feringa and co-workers comprising of bi-urea units joined *via* aliphatic and aromatic spacers; these materials have shown effective gelation behaviour in different organic solvents.[23,24] In subsequent studies, a series of light-controlled self-assembling supramolecular organogelators were developed focusing on light-triggered isomerisation between the inactive *cis* and active *trans* stiff-stilbene-type conformations, consequently resulting in reversible sol–gel photoswitching.[25,26]

The dynamic behaviour of low-molecular-weight supramolecular gels has been shown to affect the crystallisation of active pharmaceutical ingredients (APIs).[27] For example, Steed and co-workers have used the thermal triggering of supramolecular organogels to direct the crystallisation of a range of APIs, including carbamazepine (CBZ), piroxicam, sparfloxacin, and metronidazole.[28–30] In addition, the crystallisation of

[a] Department of Chemistry, University of Reading, Whiteknights, Reading RG6 6DX, UK. E-mail: w.c.hayes@reading.ac.uk
[b] Department of Chemistry, Faculty of Science, University of Zakho, Duhok 42001, Iraq
[c] Centre for Advanced Microscopy, Chemical Analysis Facility, University of Reading, Whiteknights, Reading RG6 6ED, UK
[d] Diamond Light Source, Diamond Light Source Ltd., Harwell Science & Innovation Campus, Didcot OX11 0DE, UK
[e] School of Pharmacy, University of Reading, Whiteknights, Reading RG6 6AD, UK

sulfathiazole was reported by Wang, Tao, and co-workers using linear heteropolysaccharide (agarose) as a hydrogels matrix.[31] Sanchez and co-workers employed linear amide supramolecular organogelators, which cooperatively self-assemble with biologically active molecules, to form fibrillar structures that in turn affect the crystal morphologies of a library of common APIs, such as aspirin, caffeine, indomethacin, and carbamazepine.[32]

In previous studies, we have developed hydro- and organogelators based upon the hydrogen-bonding capabilities of mono/bis-ureas which enable self-assembly in water and in a range of organic solvents.[33–37] The use of ureas in gelator systems has also been widely reported in the literature.[38–42] Low-molecular-weight urea-gelator systems have been developed *via* the reaction between bis aromatic ureas and alkyl amide spacers and these gelators show an ability to form gel phases in various organic solvents.[43] Herein, we report the design and synthesis of a series of amide-urea LMWGs that form stable and responsive nanofibergels *via* hydrogen bonding in organic media at low concentrations ($\sim$2–10 mg mL$^{-1}$). Furthermore, these LMWGs affect API polymorph crystallisation, with small structural modifications directing the generation of two novel 1 : 1 co-crystals *i.e.* chlorzoxazone (CHZ) and isonicotinamide (ISON) and chlorzoxazone and nicotinamide (NIC).

## Results and discussion

### Molecular design and synthesis of amide-urea LMWGs

Aliphatic urea-amide end-groups have previously been found to enhance the self-assembly and phase separation of supramolecular polyurethanes *via* hydrogen bonding.[44,45] Therefore, application of these functional groups as gelator systems to provide robust nanostructures upon solvation in different organic solvents was targeted. To this end, a library of aliphatic amino groups with amide functionalities has thus been designed and synthesised. The synthetic protocols used to afford these groups and the associated characterisation data are provided in the SI. The library of LMWGs (**1–3 a–f**) was accessed directly *via* reactions between the aliphatic amino-amides and the corresponding alkyl isocyanate (see Table 1 and Scheme S1). The reactions were monitored by FTIR spectroscopy to observe the consumption of the isocyanate and formation of the corresponding urea bands. All of the materials were isolated and characterised by NMR, FTIR, and mass spectrometry (see Fig. S1–S76).

The gel-formation behaviour for bis-urea compounds (**1a–1f**) and mono-urea compounds (**2a–2f** and **3a–3f**) was determined using a vial inversion protocol (see Fig. 1). A selection of apolar and polar solvents was investigated, dissolution of the gelators at various concentrations, between 0.1 wt% and 10 wt%, was achieved *via* heating, then the resulting sol was allowed to cool to room temperature. The critical gelation concentration (cgc) values were determined in those cases where gelation was observed. The cgc observations for the organogels are listed in Table 2 and Table S1.

The dynamic viscoelastic properties of the self-assembled LMWGs were assessed at a constant concentration of 10 mg mL$^{-1}$ in 1,2,4-trichlorobenzene, nitrobenzene, and DMSO. Oscillatory measurements (shear-stress, shear-strain amplitude sweep, and frequency sweep) were employed to investigate the dynamic behaviour, deformation properties, and flow of the corresponding viscoelastic LMWGs.[46] To identify the linear viscoelastic region (LVER), amplitude sweep experiments (stress and strain) were performed. The values of the storage and loss moduli, $G'$ and $G''$, respectively, are independent and when plotted as a function of applied strain or stress provided information about the gel formation (strong/weak gels and viscous sols).[30] Furthermore, to investigate the stability of the LMWGs, frequency-sweep experiments were carried out and the values of $G'$ and $G''$ were investigated as a function of the range of the applied angular frequency under a constant strain.[47] Each gelator sample was prepared by dissolving the LMWG in hot solvent then pouring it into a glass mould, which was placed onto the Peltier plate cartridge of the rheometer, obtaining a uniform disk with diameter and thickness of 10 mm and 1 mm, respectively, see Fig. S77. All the rheological experiments were performed at 25 °C.

Table 1 Chemical structures of LMWGs with different functional groups

| Derivatives | LMWGs chemical structure | | Functional amine ($RNH_2$) |
|---|---|---|---|
| **1a–f** | 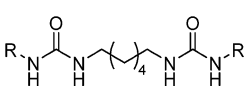 | **a** | 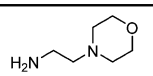 |
| | | **b** | 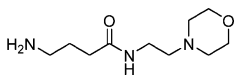 |
| **2a–f** | 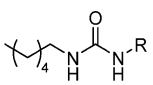 | **c** | 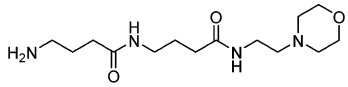 |
| | | **d** | 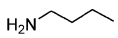 |
| | | **e** | 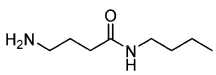 |
| **3a–f** | 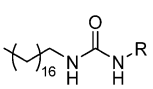 | **f** | 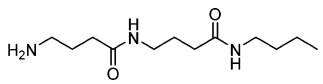 |

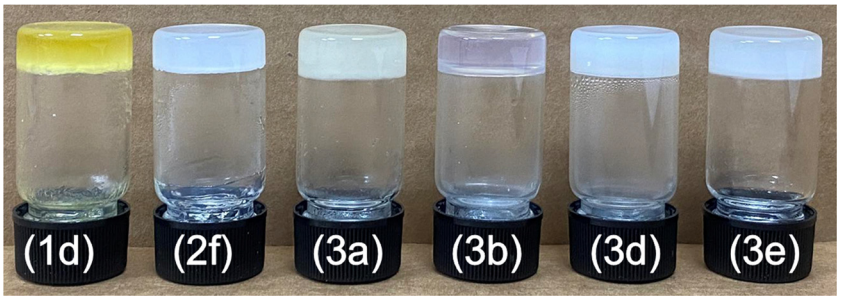


Fig. 1 Photographs showing gels obtained from the bis-urea and mono-urea LMWGs in various solvents (left to right): **1d** (nitrobenzene), **2f** (1,2,4-trichlorobenzene), **3a** (DMSO), **3b** (1,2,4-trichlorobenzene), **3d** (1,2,4-trichlorobenzene), and **3e** (DMSO) all at a concentration of 10 mg $mL^{-1}$.

Table 2 Gel screening results of the bis-urea and mono-urea gelators[a]

| Solvent | LMWG1d | LMWG2f | LMWG3a | LMWG3b | LMWG3d | LMWG3e |
|---|---|---|---|---|---|---|
| Hexane | IS | P | P | P | $G^0$ | P |
| Cyclohexane | IS | P | PG | S | PG | PG |
| 1,2,4-Trichlorobenzene | IS | $G^C$ (5 mg) | PG | $G^C$ (5 mg) | $G^C$ | $G^T$ (30 mg) |
| Toluene | P | P | P | PG | $G^0$ | PG |
| Benzene | IS | $G^C$ (1 mg) | P | $G^T$ | PG | $G^0$ |
| THF | PG | GT | P | P | $G^T$ | PG |
| $CHCl_3$ | IS | VL | S | S | S | S |
| Nitrobenzene | $G^T$ (2 mg) | S | $G^C$ | $G^C$ | S | GC |
| Dioxane | PG | $G^T$ | PG | PG | PG | PG |
| DMSO | VL | S | $G^0$ | PG | PG | $G^0$ |
| MeOH | IS | S | VL | P | S | PG |
| EtOH | IS | IS | P | P | IS | PG |
| Water | IS | VL | IS | IS | IS | IS |

[a] Abbreviations used: (IS = insoluble in the solvent under reflux, G = gel (concentration of 10 mg $mL^{-1}$, unless specified), P = precipitate, VL = viscous liquid, S = solution PG = partial gel, $G^0$ = opaque gel, $G^T$ = translucent gel, $G^C$ = transparent/clear gel).

Stress-amplitude sweep experiments were conducted from 0.001 to 100 Pa at constant frequency (1.0 Hz), see Fig. 2(A)–(C) and Fig. S78. Initially, all the LMWGs displayed viscoelastic characteristics with $G' > G''$ (by *ca.* one order of magnitude), indicating the presence of a stable gel state from the strong non-covalent interactions. **LMWG1d–3b** and **LMWG3e** showed an extended LVER from *ca.* 0.001 to 1.5 Pa, while **LMWG3d** exhibited a narrower LVER from 0.001 to 0.15 Pa. Gel–sol phase transitions occurred after the LVER region, as evident from the crossover of $G'$ and $G''$ (where $G' < G''$), resulting from the

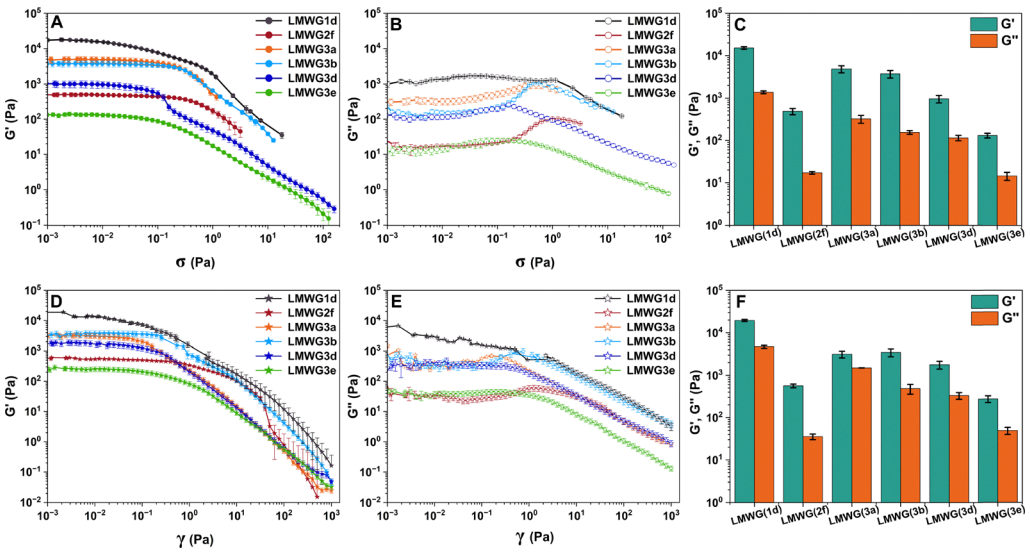


Fig. 2 Dynamic rheological property ($G'$ and $G''$) evaluation of **LMWG1d–LMWG3e**: (A)–(C) as a function of the applied shear stress, (D)–(F) as a function of the applied shear strain; standard deviation error bars were calculated from three separate measurements.

dissociation of the supramolecular networks. The strength of the gels formed from **LMWG1d–3e** can be inferred from the $G'$ values, which decrease in the order:**1d** > **3a** > **3b** > **3d** > **2f** > **3e**. In the case of **LMWG1d**, a yield stress of *ca.* $1.7 \times 10^4$ Pa suggests the formation of strong gel networks when compared to that of **LMWG3e**, where the yield stress is 2 orders of magnitude lower at $1.3 \times 10^2$ Pa. The enhanced strength of the self-assembled gel of **LMWG1d** can be attributed to the strong hydrogen-bonding interactions present in the bis-ureas, when compared to those in the mono-urea LMWG systems.

To demonstrate the dynamic behaviour of the LMWGs, oscillatory shear-strain sweep experiments were conducted from 0.001 to 1000% strain at constant frequency (1.0 Hz), see Fig. 2(D)–(F) and Fig. S79. The trend in the $G'$ magnitude values is consistent with the results from the stress-amplitude sweep experiments, with gel-to-sol phase transitions occurring from 0.4 to 40% strain. Extended LVERs were observed from 0.001 to 0.5% strain. In contrast, **LMWG2f** displays an LVER up to 40% strain owing to the strength of the hydrogen-bonding interactions between LMWG molecules. Frequency sweep experiments were carried out for LMWGs under a constant strain of 0.1%, and values of $G'$ and $G''$ were plotted as a function of applied frequency from 0.01 to 10 Hz, see Fig. S80 and S81. All the gelators displayed a solid-like nature (gel behaviour), where $G'$ dominates $G''$ (by almost one order of magnitude) and continues linearly without crossover representing high mechanical strength as a result of strong association between gelator molecules.

The rheoreversibility of a gel is an important characteristic used to measure the mechanical strength of gelators and can be demonstrated by thixotropic experiments, see Fig. 3 and Fig. S82.[48,49] A rheoreversible gel has the ability to present reversible phase transitions over several cycles, whereby a gel-to-sol transition occurs upon the application of high strain with fast reversion back to the gel state (indicating the dynamically viscoelastic nature of the gelator) when the high strain is removed.[48,50] The thixotropic behaviour of the **LMWG1d–LMWG3e** was evaluated by applying a constant low shear strain ($\gamma$ = 0.1%, frequency = 1 Hz, for 250 s) and revealed that $G' > G''$, indicating that gel nature is observed in all cases. On increasing the shear strain ($\gamma$ = 250%, frequency = 1 Hz, for 250 s) the state changed from gel to sol with $G'' > G'$ (disruption of the gelators network). In the following cycle, the shear strain was decreased from 250 to 0.1% and rapid phase transitions were observed from sol to gel phases with near complete recovery of the $G'$ and $G''$ values. The thixotropic experiments showed that all the LMWGs in their respective solvents exhibit rheoreversibility (*i.e.* self-healing), which proves the robust and dynamically reversible nature of the supramolecular networks.

Atomic force microscopy (AFM), scanning electron microscopy (SEM), and transmission electron microscopy (TEM) were

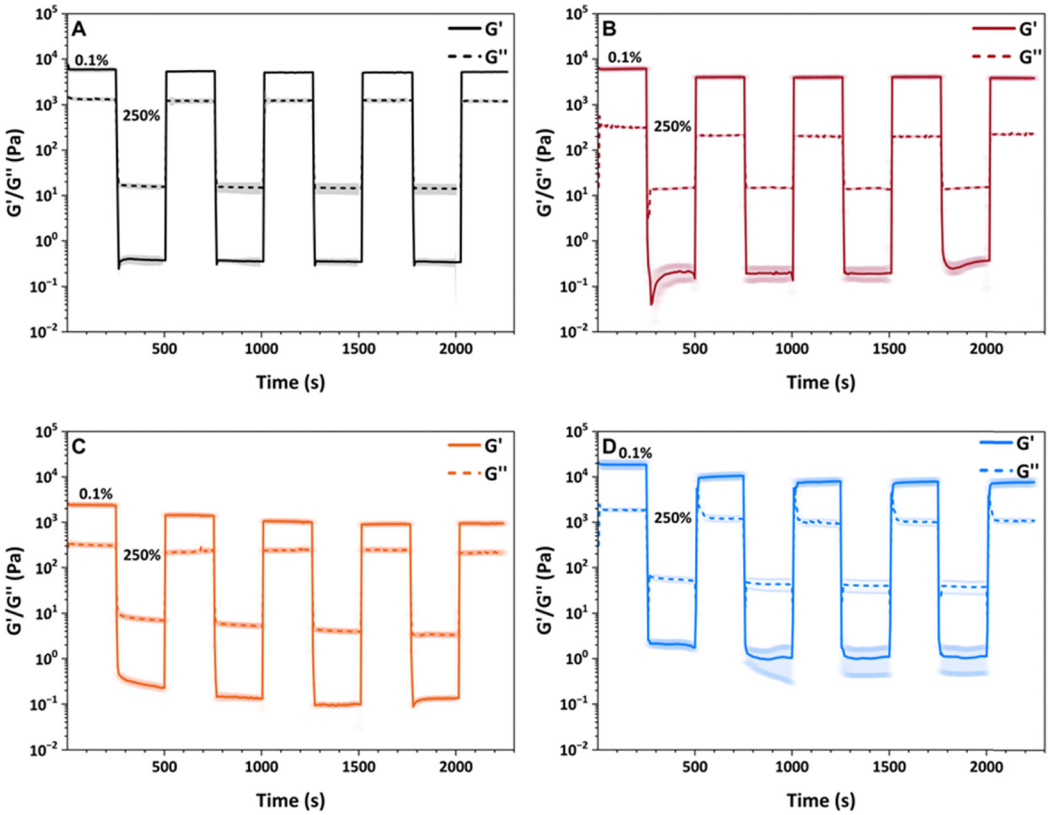


Fig. 3 Continuous step-strain measurements (thixotropic recovery) of **LMWG1d** (A), **LMWG2f** (B), **LMWG3a** (C), and **LMWG4d** (D) at 25 °C (high-amplitude oscillatory parameters: strain $\gamma$ = 250%, frequency = 1 Hz, low-amplitude oscillatory parameters: strain $\gamma$ = 0.1%, frequency = 1 Hz). The shaded regions correspond to standard deviation error bars calculated from three separate measurements.

 

used to visualise the surface and bulk morphologies of the LMWGs networks. Initial probing of the macromolecular self-assembly of the gelator networks utilised AFM in height topography-tapping mode at scale bars 5 μm, 2 μm, and 500 nm. All the xerogels of the LMWGs were prepared by drop casting from their respective solutions (0.5 mg $mL^{-1}$) onto freshly cleaved mica discs. The AFM images of **LMWG1a** and **LMWG3a** reveal long nano-fibrous networks, which are highly entangled, and nearly uniform in nature with numerous junction and twisted regions. In contrast, **LMWG2f** has irregular fibrillar networks but **LMWG3d** and **LMWG3e** possess well-defined 1D nano-rod-like morphologies without junctions which are uniform in nature with dimensions of *ca.* 265 and 286 nm (diameter), respectively. Well-developed 2D sheet morphology (big belt or lamella aggregates[51]) was evident for **LMWG3a** with dimensions of *ca.* 170 nm (height) and *ca.* 3.9 μm (diameter), see Fig. 4 and Fig. S83–S88. The variation of the surface morphology of the resulting xerogels network LMWGs may be attributed to the chemical structure,[52] self-assembly,[53] fiber aggregation,[51] intermolecular hydrophobic force,[54] and strength of the association between the gelator molecules *via* hydrogen bonds.[55]

To further ascertain how the structures of the LMWGs affect the self-assembled network, scanning electron microscopy (SEM) was performed to investigate surface morphology. The macromolecular morphologies of the **LMWG1d–LMWG3e** samples were analysed from their corresponding dried xerogels (0.5 mg $mL^{-1}$) by SEM. As shown in Fig. 4 and Fig. S89–S94, various morphologies were observed in the gelators; **LMWG1d** possesses uniform nanofibers with diameters of *ca.* 136 nm and entanglement zones. In contrast, long, thin nano-fibers with diameters of *ca.* 78 nm were observed in the case of **LMWG2f** with a significant number of junctions. This morphology explains how this gelator is able to form stable gels at low concentrations. **LMWG3a**, **LMWG3d**, and **LMWG3e** all exhibit a high density of short nano-fibers (1D nano-rod-like structures),[53] with diameters of *ca.* 68, 136 and 120 nm, respectively. The morphology of these gelators (short nano-fibers) can be directly related to the strength of the interactions between the gelator molecules in the corresponding solvents, leading to isotropic self-assembled aggregates.[56]

In addition, transmission electron microscopy (TEM) investigations were carried out on the xerogels, which further confirmed the results obtained by AFM and SEM, see Fig. 4 and Fig. S95–S100. Well-developed fibrous structures with highly entangled and dense networks were observed in **LMWG1d** and **LMWG3b**. The lengths of these fibers ranged from several hundred nanometers to micrometers and have comparable forms with a high number of junctions and twists and diameters of *ca.* 80 nm and *ca.* 116 nm, respectively. **LMWG2f** showed uniform self-assembled, elongated, rod-like structures that appear to be intertwined and interconnected to generate a star-shape aggregation, diameter *ca.* of 100 nm. These observations of the self-assembled fibers (**LMWG1d** and **LMWG3b**) or rods (**LMWG2f**) can be related to the mechanical and rheological properties of the organogels through immobilising the solvent between the gelator networks and percolating the system.[9] Furthermore, the entanglement and interactions between these fibers or rods (shorter fragments) provide the structural framework responsible for each gel's solid-like behaviour.[57] **LMWG3a** exhibits different self-assembly: big belt or lamella aggregates (diameter of *ca.* 553 nm) string together to construct the matrices. The self-assembled chains in **LMWG3d** (see Fig. 4D) showed different length fragments (nano-rod-like structures) with dimensions ranging from nanometer to micrometers that were potentially crystalline in nature, suggesting directional assembly.[58] The observed form of **LMWG3d** was likely a consequence of the sample preparation method used for TEM analysis. **LMWG3e** possesses high-density nano-fibers with many junction points (diameter of *ca.* 125 nm).

Small-angle X-ray scattering (SAXS) and wide-angle X-ray scattering (WAXS) were utilised to further the understanding of the packing, assembly, and arrangement of the molecules within the LMWG network structures in the xerogel state, see Fig. S101. SAXS measurements of **LMWG1d–LMWG3e** were fitted to a two-Lorentzian model, indicating large-scale segment aggregation with a high packing density of the molecules, see Fig. S102, S103, and Table S2. WAXS analysis of the LMWGs (Fig. S104) exhibited three prominent reflections at $q \sim 8.0$, 11.8, and 13.7 $nm^{-1}$ which correspond to *d*-spacings of *ca.* 0.7, 0.5, and 0.4 nm, respectively. Low *q* reflections are typical of nanoscale assemblies within supramolecular gels,[59] and the reflections at *ca.* 11.8 $nm^{-1}$ and 13.7 $nm^{-1}$ have previously been attributed to the hydrogen-bonded ureas and amide[60,61] within fibrillar structures. **LMWG1d** and **LMWG2f** show small additional reflections at high $q \approx 28.7$, 30.3, 33.3, and 35.1 $nm^{-1}$ corresponding to *d*-spacings of ≈0.21 nm, ≈0.20 nm, ≈0.18 nm, and ≈0.17 nm, respectively, which could be correlated to alkyl chains packing.

The crystallisation of polymorphic APIs and the selection of suitable solid-state forms are very important in pharmaceutical development.[62,63] Using LMWGs as crystallisation media has shown potential to direct and promote the growth of specific polymorphic forms of APIs.[27] Therefore, a range of different APIs (see Table 3 and Fig. S105) was investigated to assess the ability of the gelators **LMWG1d–LMWG3e** to act as crystal-growth matrices for polymorphic APIs. The morphology, type, and size of the APIs crystals can be modulated by adjusting the gelator types (composition), crystallisation period, type of solvent, and mass ratio of gelator/API. The crystallisation process of APIs in the LMWGs is presented in Scheme 1.

All the gelators (at a constant concentration 10 mg $mL^{-1}$ in the corresponding solvents) were prepared by dissolving the LMWG in the solvents to generate the sol phase. The APIs (10 mg $mL^{-1}$, 1 : 1 molar ratio for the mixed APIs) were then dissolved in their respective sol–gelators/solvent mixtures and stored at room. To monitor API crystals growth, the samples were inspected after 3, 24, and 48 hours using a stereo microscope (Fig. 5 and Fig. S106–S111). Any crystals recovered were then analysed using single-crystal X-ray diffraction, see Table S3.

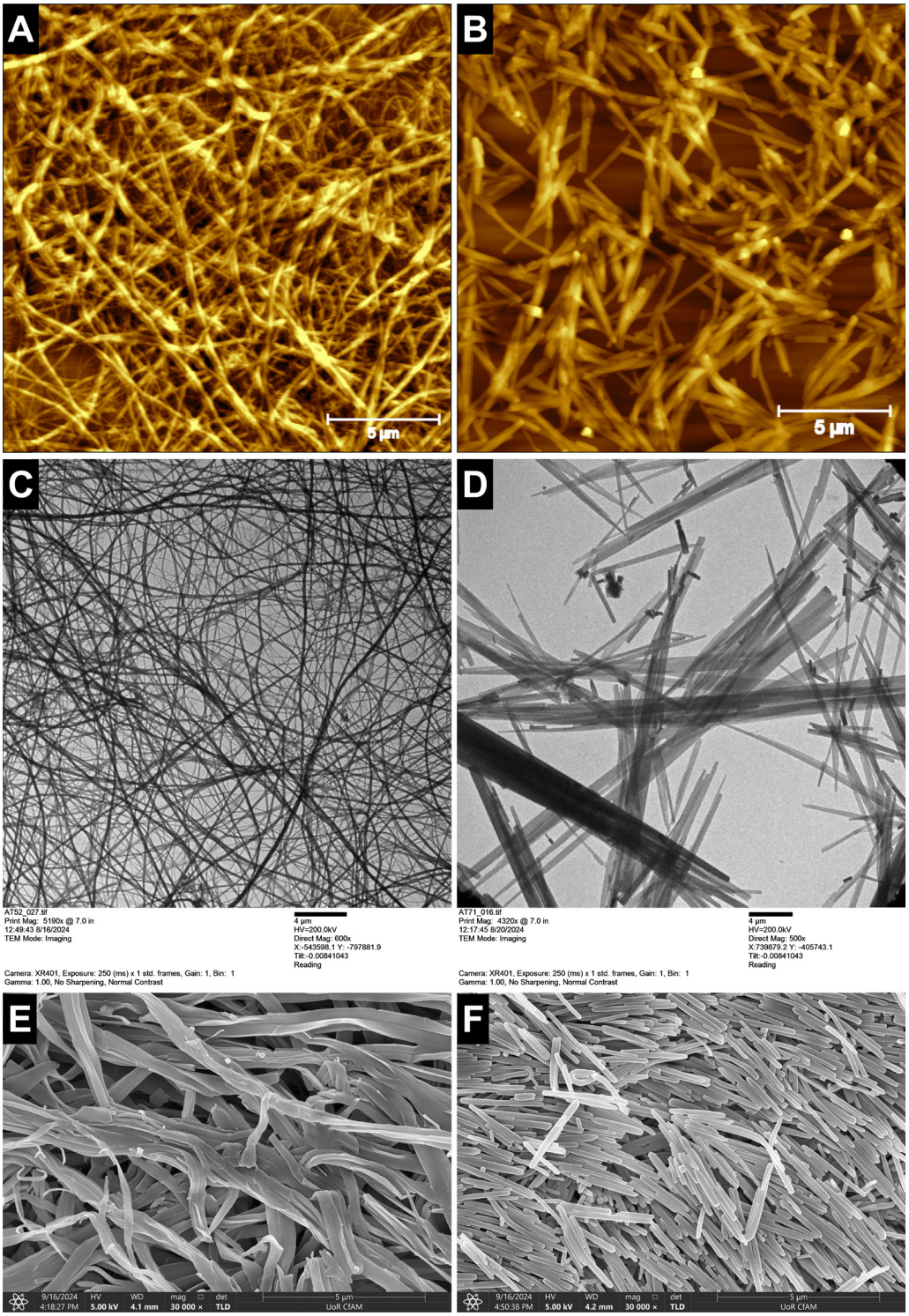


Fig. 4 AFM tapping mode height images of xerogels **LMWG1d** (A) and **LMWG3d** (B) at scale bars 5 µm, TEM images of **LMWG1d** (C) and **LMWG3d** (D) at scale bars 4 µm, and SEM images of **LMWG1d** (E) and **LMWG3d** (F) at scale bars 5 µm. The xerogel samples were drop cast from nitrobenzene for xerogel **LMWG1d** and 1,2,4-trichlorobenzene for xerogel **LMWG3d**.

Firstly, an initial screening of crystallisation was conducted for all the APIs in **LMWG1d–LMWG3e** and in non-gel solutions for reference. No crystallization of carbamazepine (CBZ) was observed in the reference samples. CBZ of polymorphic form III was produced which crystallised in either block or needle morphologies in **LMWG2f** and **LMWG3d**, while in the **LMWG3b** matrix only block-shape crystals were formed. It was noted that with **LMWG2f**, increases in CBZ concentration ($\geq$40 mg mL$^{-1}$)

 

Table 3 Crystallisation of APIs in **LMWG1d–LMWG3e** matrixes from the respective solvents

| API[a] | LMWG1d | LMWG2f | LMWG3a | LMWG3b | LMWG3d | LMWG3e |
|---|---|---|---|---|---|---|
| Carbamazepine [CBZ] | | C (III &/or II) | | C (III) | C (III &/or II) | |
| Isoniazid | C (I) | C (I) | | C (I) | C (I & II) | |
| Chlorzoxazone [CHZ] | | C (I) | C (I) | C (I) | C (I & II) | C (I & II) |
| Nicotinamide [NIC] | C (I) | C (I & II) | | C (I) | C (I) | |
| Isonicotinamide [ISON] | C (I) | C (I & II) | | C (I) | C (II) | |
| CHZ : ISON (1 : 1) | *C | | | | | C |
| CHZ : NIC (1 : 1) | | | | | *C | |

Crystallisations were carried out at a constant concentration of LMWG (10 mg $mL^{-1}$). Heating and cooling rates for samples of LMWG and APIs were consistent. C indicates instances where API crystals were observed, with specific polymorphic forms in brackets. [a] CBZ crystals (blocks) and (needles), isoniazid crystals (needles) and (plates), CHZ crystals (needles) and (rods), NIC crystals (needles) and (rods), ISON crystals (needles) and (very thin plates), * novel co-crystal CHZ : ISON (1 : 1), * novel co-crystal CHZ : NIC (1 : 1).

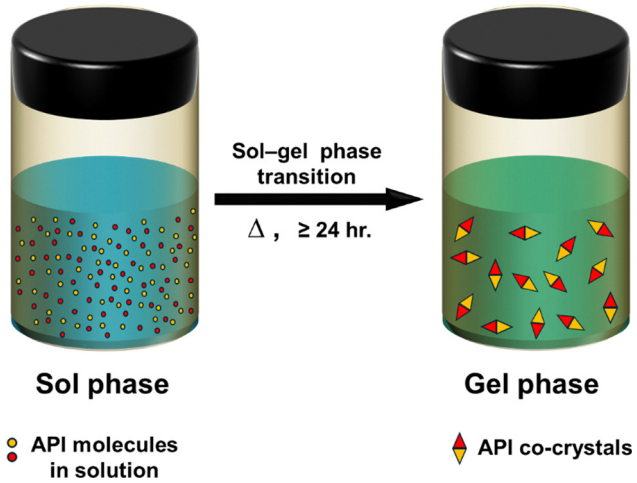


Scheme 1 Schematic representation of the sol–gel phase transition with the crystallisation of the polymorphic APIs occurring in the gelator matrix.

promoted the growth of needle-shaped crystals, whilst the growth of block-shaped crystals was suppressed.[64] In contrast, increasing the CBZ concentration enhanced the growth and size of block-shaped crystals in **LMWG3b**, which could be used as a selective crystallisation matrix for CBZ form III. **LMWG3d** produced a mixture of form II and III crystals irrespective of the concentration of CBZ.

Needle-like morphology crystals of isonicotinic acid hydrazide (isoniazid) form I were observed[65] in **LMWG1d**, **LMWG2f**, **LMWG3b**, **LMWG3d**, and in the reference samples. Highly dense and large sized needle-like crystals were generated after increasing the concentration of the isoniazid in the LMWG matrices. Furthermore, clusters of needles of CHZ appeared[66] in **LMWG2f–LMWG3e** after 3 hours. Crystals of similar morphology were still present at room temperature after 24 hours, but crystallisation was not observed in the non-gel samples. The crystallisation of NIC and ISON was observed in the same type of gelator media (**LMWG1d**, **LMWG2f**, **LMWG3b**, and **LMWG3d**) and in the non-gel samples (1,2,4-trichlorobenzene). NIC crystals were obtained as needles[67] in **LMWG3b** and **LMWG3d**, while use of **LMWG2f** as the matrix afforded thin plate-like crystals and needles which were larger in size than those obtained from **LMWG3b** and **LMWG3d**. Interestingly, many junctions between trees of needle-like crystals NIC were observed in **LMWG1d**. The nature of the nucleation of ISON crystals in **LMWG1d** resulted in needle-shaped crystals. Remarkably, branched needle-like crystals

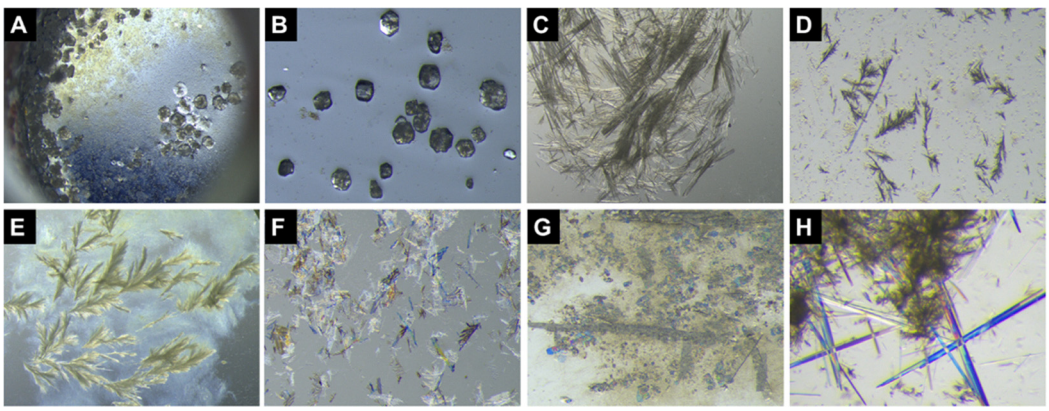


Fig. 5 Morphology of the API crystals in 1 wt% LMWGs, (A) and (B) CBZ in **LMWG3b** (1,2,4-trichlorobenzene) ×7.5 and ×12 magnification, respectively, (C) isoniazid in **LMWG3b** (1,2,4-trichlorobenzene) ×7.5 magnification, (D) CHZ in **LMWG3e** (1,2,4-trichlorobenzene) ×24 magnification, (E) NIC in **LMWG1d** (nitrobenzene) ×7.5 magnification, (F) ISON (1 : 1 mole) in **LMWG3b** (1,2,4-trichlorobenzene) ×12 magnification after 3 hours, (G) CHZ : ISON (1 : 1) in **LMWG1d** (nitrobenzene) ×15 magnification, and (H) CHZ : NIC (1 : 1) in **LMWG3d** (1,2,4-trichlorobenzene) 30 magnification.

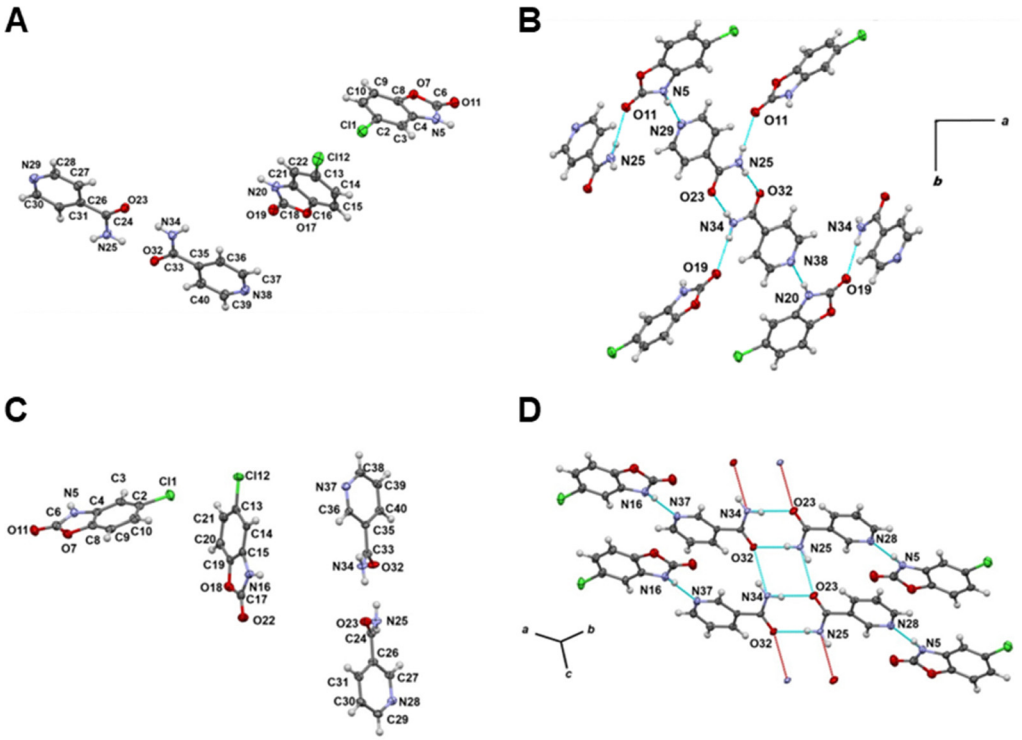


Fig. 6 (A) There are four molecules in the asymmetric unit of CHZ : ISON (1 : 1) (B) view along the *c* axis showing the hydrogen-bonding interactions (pale-blue lines) between the four molecules in the asymmetric unit. The R2,2,(8) motif formed by the two isonicotinamides of the asymmetric unit is clearly visible, (C) there are four molecules in the asymmetric unit of CHZ : NIC (1 : 1), and (D) view showing the hydrogen-bonding interactions (pale-blue lines) between the four molecules in the asymmetric unit.

appeared consistently when crystallised in **LMWG2f** and **LMWG3b**, **LMWG3d**.

A novel CHZ : ISON (1 : 1) co-crystal was obtained within the **LMWG1d** matrix (see Fig. 6A), forming large rod-like crystals alongside smaller grains after 3 hours. No co-crystal formation was observed in the corresponding non-gel reference. The initial grains developed into large rod- and plate-like crystals after 24 hours within the **LMWG1d** matrix at room temperature. Additionally, large co-crystals with the same lattice parameters as CHZ : ISON (1 : 1), but with a plate-like morphology was observed in the **LMWG3e** matrix after both 3 and 24 hours.

There are two molecules of isonicotinamide and two molecules of chlorzoxazone in the asymmetric unit (Fig. 6A) of the new cocrystal CHZ : ISON (1 : 1). The molecules pack together to form a 3-D structure that features an extensive network of hydrogen bonding (Fig. 6B); a full graph set analysis of the structure is given in Tables S4–S7.

The co-crystallisation of chlorzoxazone and nicotinamide in LMWGs resulted in the formation of a novel CHZ : NIC (1 : 1) co-crystal. Formed in **LMWG3d**, presenting as rods-like crystals after 24 hours inside the gelator matrix, the molecules pack together to form a 3-D structure held together by a network of hydrogen bonding interactions, a full graph set analysis of the structure is given in Tables S8–S11. Additionally, co-crystals were not observed in the reference samples, with only crystals of nicotinamide present.

## Conclusions

This study demonstrates how the design of LMWGs can be exploited to tune self-assembled nanostructured gel morphologies to enable the selective crystallisation of APIs of specific polymorphic forms. Self-assembly *via* hydrogen-bonding interactions of the LMWGs form mechanically robust gels at 0.1–10 wt% in a range of organic solvents, with fibers, big belt or lamella sheets, and 1D rod-like nanostructured morphologies. Utilisation of the LMWGs as crystallisation matrices for a library of polymorphic APIs was explored, ultimately enabling the selective isolation of specific forms. The co-crystallization of APIs was also achieved using the LMWG matrices enabling the isolation of novel CHZ : NIC (1 : 1) and CHZ : ISON (1 : 1) co-crystals. These results underscore the ability for these LMWG to influence and direct polymorph and co-crystal generation through the design of self-assembled nanostructured gelators. Currently, these gels are best viewed as tools for crystallisation screens, as bulk retrieval of crystals from the gel matrices remains an issue.

## Experimental section

### Materials

All the starting materials and reagents were purchased from Sigma Aldrich, Tokyo Chemical Industry (TCI), and Fisher Chemical and used as received. Tetrahydrofuran (THF) was

dried by using an MBRAUN SP7 system fitted with activated alumina columns. CHZ was identified by powder X-ray diffraction as being the triclinic form (*e.g.* CSD refcode NEWKOP); NIC was similarly identified as being monoclinic form I (*e.g.* CSD refcode NICOAM01) and ISON was monoclinic form II (CSD refcode EHOWIH02).

### Characterisation

$^{1}$H NMR and $^{13}$C NMR spectra were both measured using either a Bruker Nanobay 400 or a Bruker DPX 400 spectrometer operating at 400 MHz ($^{1}$H NMR) or 100 MHz ($^{13}$C NMR). Chemical shifts ($\delta$) are reported in ppm relative to the residual solvent resonance for $CDCl_3$ ($\delta$ 7.26 ppm) or DMSO-$d_6$ ($\delta$ 2.50 ppm). Fourier-transform infrared (FTIR) spectroscopic analysis was carried out at room temperature using a PerkinElmer 100 FTIR instrument equipped with a diamond-ATR sampling accessory. Mass spectrometry (MS) was conducted using a Thermo Fisher Scientific Orbitrap XL LCMS. The sample was introduced by liquid chromatography (LC) and sample ionisation achieved by electrospray ionisation (ESI). Gel-state rheological measurements were performed on a Malvern Panalytical Kinexus Lab+ instrument fitted with a Peltier plate cartridge and 20 mm parallel plate geometry and analysed using rSpace Kinexus v1.76.2398 software. Optical microscopy images of the crystallised APIs were taken using a Leica M80 stereo microscope with magnification range from $\times$7.5 to $\times$60 when equipped with a $\times$1 objective, $\times$10 eyepieces and Leica IC80 camera.

Single-crystal X-ray diffraction data were collected using a Rigaku XtaLAB Synergy diffractometer (Cu $K_\alpha$ radiation, $\lambda$ = 1.54184 Å). API crystals were mounted in Paratone-N oil and cooled to 100 K by an Oxford Cryosystems Cryostream. X-ray data were reduced using CrysAlisPro software[68] and the structures solved using the Superflip;[69] all non-hydrogen atoms were located. Least-squares refinement against $F^2$ was carried out using the CRYSTALS suite[70] with all non-hydrogen atoms refined anisotropically and hydrogen atoms located in difference Fourier maps. The positions of the hydrogen atoms attached to nitrogen were refined with a $U_{iso}$ of $\sim$1.2–1.5 times the value of $U_{eq}$ of the parent N atom. Hydrogen atoms attached to carbon were placed geometrically with a C–H distance of 0.95 Å and a $U_{iso}$ of $\sim$1.2–1.5 times the value of $U_{eq}$ of the parent C atom, and the positions refined with riding constraints.[71]

Small-angle X-ray scattering (SAXS) and wide-angle X-ray scattering (WAXS) experiments were performed on a Bruker SAXS Nanostar at University of Reading, with Incoatec Microfocus Source IμS with an energy of 8.04 keV corresponding to a wavelength of 1.54 Å. Data were collected using a photon counting Vantec 500 detector with sample to detector length of 66 cm. The beam size was 0.5 mm in diameter on the sample. Silver behenate (layer spacing, $d$ = 58.38 Å) was used to calibrate the SAXS data, LMWGs samples were cast onto Kapton™ films and SAXS patterns were measured for 4 hours. The SAXS images were analysed using DAWN software and SAXS fitting was achieved using SasView Version 5.0.6 (https://www.sasview.org) using a shape-independent category two-Lorentzian function.

The scattering intensity ($I$) in a shape-independent two-Lorentzian model is calculated as:

$$I(q) = \frac{A}{1 + (Q\xi_1)^n} + \frac{C}{1 + (Q\xi_2)^m} + B$$

where: $A$ = Lorentzian scale factor #1, $C$ = Lorentzian scale #2, $\xi_1$ and $\xi_2$ are the corresponding correlation lengths, and $n$ and $m$ are the respective power-law exponents (set $n = m = 2$ for Ornstein–Zernicke behaviour).

$d$-Spacings were calculated using the following equation:

$$d = \frac{2\pi}{q_0}$$

Atomic force microscopy (AFM) images were obtained using a Cypher S AFM (Oxford Instruments-Asylum Research, Santa Barbara, USA) at University of Reading. The AFM stage movements within the $x$, $y$ and $z$ directions were controlled using piezoelectric stacks. The scans were recorded through the user interface, Igor Pro (Version 16.33.234), using the standard alternating contact (AC) topography mode (tapping mode) operating in air using a silicon tip with a resonant frequency set at approximately 70 kHz and a spring constant of approximately 2.0 $Nm^{-1}$ (AC240TS-R3, Oxford Instruments). Each sample was drop cast onto a 10 mm diameter AFM mica disc, which had been first cleaved with Sellotape. Each disc was then mounted onto 15 mm diameter magnetic stainless steel AFM specimen disc using 9 mm diameter carbon adhesive tabs and secured onto the microscope scanner stage magnetically. Then, through the user interface, the objective focus was adjusted and set to focus on the tip and on each sample in turn. The cantilever was autotuned at its resonance which automatically determined the drive amplitude and drive frequency. The resolution, scan rate, integral gain and scan size were entered into the user interface before starting the scan. The software Gwyddion (version 2.63, https://gwyddion.net)) was used for data analysis and editing.

Scanning electron microscopy (SEM) images were taken using a Thermo Helios 5 CX FIB-SEM. Samples were examined under high vacuum conditions with an accelerating voltage of 5 kV and a working distance of approximately 4 mm. Each sample was drop cast from their corresponding solvent (sol phase) onto a glass slide and dried over five days at room temperature. The dried xerogel samples were carefully placed onto carbon adhesive discs (12.5 mm diameter) that were mounted onto aluminium SEM pin stubs of 12.5 mm diameter. A thin layer of gold particles was then sputtered onto the surface using an Edwards S150B sputter coater (1.5 minutes coat with the stub placed angled on its side, then rotated 180° and coated for another 1.5 minutes). The average diameter of the fibers/sheets/rods was calculated using an image analysis tool, ImageJ (version 1.5, https://imagej.net).

Transmission electron microscopy (TEM) images were obtained using a JEOL JEM-2100Plus at an accelerating voltage of 200 kV. The gelators were dissolved in their corresponding solvents at a concentration of 0.5 mg $mL^{-1}$ *via* heating and

drop cast onto pure carbon films on 300 mesh copper grids, samples were then allowed to dry under vacuum at room temperature for two days. The grids were observed without any staining and ImageJ 1.5v. was used to measure the diameters of the fibers, sheets/and rods.

## Author contributions

Alarqam Z. Tareq: conceived the work, designed and performed the experiments, investigation, and writing – original draft; Matthew Hyder: conceptualisation, investigation, and writing – reviewing and editing. Ann M. Chippindale: interpreted the X-ray crystallographic measurements, reviewing, and editing. Nicholas J. Spencer: collected the X-ray data. Saeed D. Mohan and Amanpreet Kaur: collected the SEM and TEM. James E. Hallett: investigation – SAXS and WAXS. Thomas Zinn: investigation – SAXS and WAXS. Kenneth Shankland: investigation – APIs selection, interpretation of crystal structures, reviewing, and editing. Wayne Hayes: supervised the project, writing – reviewing, editing and contributed to the manuscript. All authors reviewed the manuscript.

## Conflicts of interest

There are no conflicts to declare.

## Data availability

The data supporting this article have been included as part of the supplementary information (SI). Supplementary information: further information regarding detailed synthetic procedures, protection, coupling, and deprotection protocols; additional characterisation data for the LMWGs, including NMR, FTIR, MS, rheological experiments, single-crystal XRD, SAXS, WAXS, microscopic images of crystals APIs, additional AFM, SEM, and TEM images. See DOI: https://doi.org/10.1039/d6tb00302h.

CCDC 2468350 and 2490051 contain the supplementary crystallographic data for this paper.[71a,b]

## Acknowledgements

The authors would like to acknowledge the financial support from HCED Iraq (PhD studentship for A. Tareq) and from the University of Reading and Domino Printing Sciences Ltd (PhD studentship for M. Hyder). In addition, the University of Reading is acknowledged for providing access to instrumentation in the Chemical Analysis Facility. The authors also thank Diamond Light Source for the award of SAXS lab. time, ref SM40382-1.

## References

1 C. D. Jones and J. W. Steed, *Chem. Soc. Rev.*, 2016, **45**, 6546–6596.
2 J. H. van Esch, *Langmuir*, 2009, **25**, 8392–8394.
3 X. Yan, F. Wang, B. Zheng and F. Huang, *Chem. Soc. Rev.*, 2012, **41**, 6042–6065.
4 Z.-X. Liu, Y. Feng, Z.-C. Yan, Y.-M. He, C.-Y. Liu and Q.-H. Fan, *Chem. Mater.*, 2012, **24**, 3751–3757.
5 V. J. Nebot, J. J. Ojeda-Flores, J. Smets, S. Fernández-Prieto, B. Escuder and J. F. Miravet, *Chem. – Eur. J.*, 2014, **20**, 14465–14472.
6 F. Rodríguez-Llansola, B. Escuder, J. F. Miravet, D. Hermida-Merino, I. W. Hamley, C. J. Cardin and W. Hayes, *Chem. Commun.*, 2010, **46**, 7960–7962.
7 W. Deng, H. Yamaguchi, Y. Takashima and A. Harada, *Chem. Commun.*, 2007, 5144–5147.
8 E. R. Draper and D. J. Adams, *Chem*, 2017, **3**, 390–410.
9 P. Terech and R. G. Weiss, *Chem. Rev.*, 1997, **97**, 3133–3160.
10 R. G. Weiss, *J. Am. Chem. Soc.*, 2014, **136**, 7519–7530.
11 N. M. Sangeetha and U. Maitra, *Chem. Soc. Rev.*, 2005, **34**, 821–836.
12 J. H. Fuhrhop, P. Schnieder, J. Rosenberg and E. Boekema, *J. Am. Chem. Soc.*, 1987, **109**, 3387–3390.
13 N. Bajaj, L. R. Hart, B. W. Greenland and W. Hayes, *Macromol. Symp.*, 2013, **329**, 118–124.
14 N. Cheng, Q. Kang, J. Xiao, N. Du and L. Yu, *J. Colloid Interface Sci.*, 2018, **511**, 215–221.
15 M. Lescanne, P. Grondin, A. d'Aléo, F. Fages, J. L. Pozzo, O. M. Monval, P. Reinheimer and A. Colin, *Langmuir*, 2004, **20**, 3032–3041.
16 D. Yang, S. Xia, M. Bao, X. Chen, H. Kang, H. Zhao and Y. Li, *J. Mater. Chem. A*, 2023, **11**, 6181–6190.
17 T. Yi, X. Yu and L. Chen, in *Hydrogen Bonded Supramolecular Materials*, ed. Z.-T. Li and L.-Z. Wu, Springer Berlin Heidelberg, Berlin, Heidelberg, 2015, pp. 69–100.
18 R. Custelcean, *Chem. Commun.*, 2008, 295–307.
19 B. Escuder and J. F. Miravet, *Functional Molecular Gels,* The Royal Society of Chemistry, 2013, pp. 304–319.
20 L. Fischer and G. Guichard, *Org. Biomol. Chem.*, 2010, **8**, 3101–3117.
21 W. J. Peveler, H. Packman, S. Alexander, R. R. Chauhan, L. M. Hayes, T. J. Macdonald, J. K. Cockcroft, S. Rogers, D. G. A. L. Aarts, C. J. Carmalt, I. P. Parkin and J. C. Bear, *Soft Matter*, 2018, **14**, 8821–8827.
22 M. Fernández-Castaño Romera, X. Lou, J. Schill, G. ter Huurne, P.-P. K. H. Fransen, I. K. Voets, C. Storm and R. P. Sijbesma, *J. Am. Chem. Soc.*, 2018, **140**, 17547–17555.
23 J. van Esch, S. De Feyter, R. M. Kellogg, F. De Schryver and B. L. Feringa, *Chem. – Eur. J.*, 1997, **3**, 1238–1243.
24 J. van Esch, R. M. Kellogg and B. L. Feringa, *Tetrahedron Lett.*, 1997, **38**, 281–284.
25 S. J. Wezenberg, C. M. Croisetu, M. C. A. Stuart and B. L. Feringa, *Chem. Sci.*, 2016, **7**, 4341–4346.
26 F. Xu, L. Pfeifer, S. Crespi, F. K.-C. Leung, M. C. A. Stuart, S. J. Wezenberg and B. L. Feringa, *J. Am. Chem. Soc.*, 2021, **143**, 5990–5997.
27 H. Sharma, B. K. Kalita, D. Pathak and B. Sarma, *Cryst. Growth Des.*, 2024, **24**, 17–37.

 

28 K. Fucke, A. J. Edwards, M. R. Probert, S. E. Tallentire, J. A. K. Howard and J. W. Steed, *ChemPhysChem*, 2013, **14**, 675–679.
29 J. A. Foster, M.-O. M. Piepenbrock, G. O. Lloyd, N. Clarke, J. A. K. Howard and J. W. Steed, *Nat. Chem.*, 2010, **2**, 1037–1043.
30 S. S. Jayabhavan, J. W. Steed and K. K. Damodaran, *Cryst. Growth Des.*, 2021, **21**, 5383–5393.
31 S. Song, L. Wang, C. Yao, Z. Wang, G. Xie and X. Tao, *Cryst. Growth Des.*, 2020, **20**, 9–16.
32 F. Aparicio, E. Matesanz and L. Sánchez, *Chem. Commun.*, 2012, **48**, 5757–5759.
33 A. D. Odonnell, A. G. Gavriel, W. Christie, A. M. Chippindale, I. M. German and W. Hayes, *ARKIVOC*, 2021, **2021**, 222–241.
34 B. C. Baker, C. L. Higgins, D. Ravishankar, H. M. Colquhoun, G. C. Stevens, F. Greco, B. W. Greenland and W. Hayes, *ChemistrySelect*, 2016, **1**, 1641–1649.
35 D. M. Wood, B. W. Greenland, A. L. Acton, F. Rodríguez-Llansola, C. A. Murray, C. J. Cardin, J. F. Miravet, B. Escuder, I. W. Hamley and W. Hayes, *Chem. – Eur. J.*, 2012, **18**, 2692–2699.
36 F. Rodríguez-Llansola, D. Hermida-Merino, B. Nieto-Ortega, F. J. Ramírez, J. T. L. Navarrete, J. Casado, I. W. Hamley, B. Escuder, W. Hayes and J. F. Miravet, *Chem. – Eur. J.*, 2012, **18**, 14725–14731.
37 F. Rodríguez-Llansola, B. Escuder, I. W. Hamley, W. Hayes and J. F. Miravet, *Soft Matter*, 2012, **8**, 8865–8872.
38 A. J. P. Teunissen, M. M. L. Nieuwenhuizen, F. Rodríguez-Llansola, A. R. A. Palmans and E. W. Meijer, *Macromolecules*, 2014, **47**, 8429–8436.
39 N. Mohmeyer and H.-W. Schmidt, *Chem. – Eur. J.*, 2005, **11**, 863–872.
40 B. O. Okesola and D. K. Smith, *Chem. Soc. Rev.*, 2016, **45**, 4226–4251.
41 N. E. Botterhuis, S. Karthikeyan, A. J. H. Spiering and R. P. Sijbesma, *Macromolecules*, 2010, **43**, 745–751.
42 J. W. Steed, *Chem. Commun.*, 2011, **47**, 1379–1383.
43 B. C. Baker, A. L. Acton, G. C. Stevens and W. Hayes, *Tetrahedron*, 2014, **70**, 8303–8311.
44 A. Z. Tareq, M. Hyder, D. H. Merino, A. M. Chippindale, A. Kaur, J. A. Cooper and W. Hayes, *Polymer*, 2024, **302**, 127052.
45 A. Z. Tareq, M. Hyder, D. H. Merino, S. D. Mohan, J. A. Cooper and W. Hayes, *Eur. Polym. J.*, 2025, **228**, 113782.
46 D. A. Tómasson, D. Ghosh, M. R. P. Kurup, M. T. Mulvee and K. K. Damodaran, *CrystEngComm*, 2021, **23**, 617–628.
47 M. Kuddushi, A. Kumar, D. Ray, V. K. Aswal, O. A. El Seoud and N. I. Malek, *ACS Omega*, 2020, **5**, 24272–24284.
48 X. Huang, S. R. Raghavan, P. Terech and R. G. Weiss, *J. Am. Chem. Soc.*, 2014, **136**, 13072.
49 C. K. Karan and M. Bhattacharjee, *ACS Appl. Mater. Interfaces*, 2016, **8**, 5526–5535.
50 A. R. Patel, M. Babaahmadi, A. Lesaffer and K. Dewettinck, *J. Agric. Food Chem.*, 2015, **63**, 4862–4869.
51 G. Zhu and J. S. Dordick, *Chem. Mater.*, 2006, **18**, 5988–5995.
52 H.-K. Yang, C. Zhang, X.-N. He and P.-Y. Wang, *Colloids Surf., A*, 2021, **616**, 126319.
53 X. Y. Liu, P. D. Sawant, W. B. Tan, I. B. M. Noor, C. Pramesti and B. H. Chen, *J. Am. Chem. Soc.*, 2002, **124**, 15055–15063.
54 M. Kogiso, S. Ohnishi, K. Yase, M. Masuda and T. Shimizu, *Langmuir*, 1998, **14**, 4978–4986.
55 T. Shimizu and M. Masuda, *J. Am. Chem. Soc.*, 1997, **119**, 2812–2818.
56 Y. Yu, S. Wang, L. Jia, M. Zhou, Q. Pan, Y. Zhai and C. Wang, *J. Sol-Gel Sci. Technol.*, 2016, **78**, 218–227.
57 J.-K. Kim, J. Anderson, H.-W. Jun, M. A. Repka and S. Jo, *Mol. Pharmaceutics*, 2009, **6**, 978–985.
58 H. Wang, Y. Han, W. Yuan, M. Wu and Y. Chen, *Chem. – Asian J.*, 2018, **13**, 1173–1179.
59 G. Campi, L. Suber, G. Righi, L. Primitivo, M. De Angelis, D. Caschera, L. Pilloni, A. Del Giudice, A. Palma, M. Satta, A. Fortunelli and L. Sementa, *Nanoscale Adv.*, 2021, **3**, 2948–2960.
60 R. Sattler, V. Danke and M. Beiner, *Macromol. Chem. Phys.*, 2023, **224**, 2200433.
61 B. Lotz, *Macromolecules*, 2021, **54**, 551–564.
62 J. Chen, B. Sarma, J. M. B. Evans and A. S. Myerson, *Cryst. Growth Des.*, 2011, **11**, 887–895.
63 D. Erdemir, A. Y. Lee and A. S. Myerson, *Acc. Chem. Res.*, 2009, **42**, 621–629.
64 H. Yang, C. L. Song, Y. X. S. Lim, W. Chen and J. Y. Y. Heng, *CrystEngComm*, 2017, **19**, 6573–6578.
65 L. H. Jensen, *J. Am. Chem. Soc.*, 1954, **76**, 4663–4667.
66 S. İde and A. Topaçh, *J. Chem. Crystallogr.*, 1997, **27**, 303–306.
67 L. Fábián, N. Hamill, K. S. Eccles, H. A. Moynihan, A. R. Maguire, L. McCausland and S. E. Lawrence, *Cryst. Growth Des.*, 2011, **11**, 3522–3528.
68 O. D. Rigaku, *P. R. O. CrysAlis*, Rigaku Oxford Diffraction Ltd, Yarnton, Oxfordshire, England, 2019.
69 L. Palatinus and G. Chapuis, *J. Appl. Crystallogr.*, 2007, **40**, 786–790.
70 P. W. Betteridge, J. R. Carruthers, R. I. Cooper, K. Prout and D. J. Watkin, *J. Appl. Crystallogr.*, 2003, **36**, 1487.
71 (*a*) CCDC 2468350: Experimental Crystal Structure Determination, 2026, DOI: 10.5517/ccdc.csd.cc2nvj68; (*b*) CCDC 2490051: Experimental Crystal Structure Determination, 2026, DOI: 10.5517/ccdc.csd.cc2pl37n.